



Design and implementation of a particle image velocimetry method for analysis of running gear–soil interaction

Carmine Senatore^{a,*}, Markus Wulfmeier^a, Ivan Vlahinić^b, Jose Andrade^b, Karl Iagnemma^a

^a *Laboratory for Manufacturing and Productivity, Massachusetts Institute of Technology, Cambridge, MA 02139, USA*

^b *Department of Mechanical and Civil Engineering, California Institute of Technology, Pasadena, CA 91125, USA*

Received 24 October 2012; received in revised form 2 July 2013; accepted 29 September 2013

Available online 20 October 2013

Abstract

Experimental analysis of running gear–soil interaction traditionally focuses on the measurement of forces and torques developed by the running gear. This type of measurement provides useful information about running gear performance but it does not allow for explicit investigation of soil failure behavior. This paper describes a methodology based on particle image velocimetry for analyzing soil motion from a sequence of images. A procedure for systematically identifying experimental and processing settings is presented. Soil motion is analyzed for a rigid wheel traveling on a Mars regolith simulant while operating against a glass wall, thereby imposing plain strain boundary conditions. An off-the-shelf high speed camera is used to collect images of the soil flow. Experimental results show that it is possible to accurately compute soil deformation characteristics without the need of markers. Measured soil velocity fields are used to calculate strain fields.

© 2013 ISTVS. Published by Elsevier Ltd. All rights reserved.

Keywords: Granular particle image velocimetry; Terrain shearing failure; Wheel dynamics; Off-road vehicle performance

1. Introduction

Particle image velocimetry (PIV) describes an experimental method, based on image cross-correlation techniques, used for the determination of flow velocity fields. The use of PIV for the calculation of fluid velocities initially emerged in the 1980s [1,2]. Since then, PIV has played an important role in many fluid mechanics investigations [3,4]. Two of the main advantages of PIV over other methods for the measurement of velocity (e.g. hot-wire-velocimetry, Pitot tubes, etc.) are that it is non-intrusive, and allows for relatively high resolution measurements over an extended spatial domain.

During fluid-based PIV analysis, the fluid is typically seeded with marker particles that refract, absorb, or

scatter light, have a high contrast with the fluid, and do not interrupt the fluid flow. Imaging is performed at high speed over an area of the flow illuminated by a light source, typically a pulsed laser. The resulting light sheet can be considered as being nearly two-dimensional, because of its low propagation orthogonal to the plane of measured motion [5]. Lasers are typically chosen as light sources because of their ability to emit high-energy, monochromatic light as thin light sheets. Captured images are processed with algorithms that perform frame-to-frame feature tracking and calculation of flow velocity fields.

PIV is also a useful method for measuring soil motion, with the notable constraint that soil is typically observed through a glass sheet, limiting the resulting analysis to plain strain scenarios. The natural granular texture of soils often generates an intensity pattern that can be traced by PIV, without the use of marker particles. Also, incandescent light can generally be used for illumination. Although the term PIV is traditionally associated with fluid

* Corresponding author.

E-mail addresses: senator@mit.edu (C. Senatore), markusw@mit.edu (M. Wulfmeier), ivan@caltech.edu (I. Vlahinić), jandrade@caltech.edu (J. Andrade), kdi@mit.edu (K. Iagnemma).

mechanics investigation (and the corresponding experimental setup), here we will use the term to refer to the general concept of extracting velocity fields from sequences of images. This is sometimes referred to as digital image correlation.

Granular PIV has recently been employed in several applications, including the analysis of grains in converging hoppers [6], study of flowing granular layers in rotating tumblers [7], investigation of granular avalanches [8], analysis of soil motion caused by the movement of animals [9], the study of burrowing behavior of razor clams [10], and in the study of wheel-soil interaction [11,12]. The analysis of soil motion beneath a driven wheel via quantitative analysis of successive temporal images was first introduced by Wong [13]. However, the experimental capabilities of that study did not allow for high-speed image capture, limiting the accuracy and practical utility of the method.

This paper describes a systematic PIV-based methodology for analyzing soil motion beneath a running gear (i.e. wheel, track, limb, etc.). A procedure for determining hardware and software operational parameters is presented, and various useful techniques for quantitatively analyzing soil failure are presented. The case of interest in this paper is that of Mars surface exploration by small, lightweight wheeled rovers. Experimental results are thus presented for a rigid wheel traveling on a Mars regolith simulant. A high speed camera is used to collect images of the soil flow. Experimental results show that it is possible to compute, with satisfactory accuracy, soil deformation characteristics without the need of markers.

The paper is organized as follows: the section entitled “Particle image velocimetry for granular material” presents a thorough description of experimental setup and a lean introduction on PIV parameter identification. This section also contains validation and verification experiments, and introduces a methodology for inferring strain fields from the measured velocity fields. The section “Application to analysis of running gear–soil interaction” shows how PIV can be used to qualitatively and quantitatively study soil failure mechanism under running gears. Details on PIV parameter identification and procedures are presented in [Appendix A](#).

2. Particle image velocimetry for granular materials

In this section, a through description of the experimental apparatus is presented and a brief overview of PIV procedures is introduced. Note that in the following, the Matlab-based PIVlab software package is employed [14]. Details on how to identify operational parameters for PIVlab can be found in [Appendix A](#).

2.1. Testbed description

The Robotic Mobility Group at MIT has designed and fabricated a multipurpose terramechanics rig based on the standard design described in [15].

The testbed is pictured in [Fig. 1](#). It is composed of a Lexan soil bin surrounded by an aluminum frame to which all the moving parts, actuators and sensors are attached. A carriage slides on two low-friction rails to allow longitudinal translation while the wheel or track, attached to the carriage, is able to rotate at a desired angular velocity. The wheel mount is also able to translate in the vertical direction. This setup allows control of slip and vertical load by modifying the translational velocity of the carriage, angular velocity of the wheel, and applied load. Horizontal carriage displacement is controlled through a toothed belt, actuated by a 90 W Maxon DC motor, while the wheel is directly driven by another Maxon DC motor. The motors are controlled through two identical Maxon ADS 50/10 4-Q-DC servo-amplifiers. The carriage horizontal displacement is monitored with a Micro Epsilon WPS-1250-MK46 draw wire encoder while wheel vertical displacement (i.e., sinkage) is measured with a Turck A50 draw wire encoder. A 6-axis force/torque ATI Omega 85 transducer is mounted between the wheel mount and the carriage in order to measure vertical load and traction generated by the wheel. Finally, a Futek TFF500 flange-to-flange reaction torque sensor is used to measure driving torque applied to the wheel. Control and measurement signals are handled by a NI PCIe-6363 card through Labview software.

The rig is capable of approximately 1 meter of longitudinal displacement at a maximum velocity of approximately 0.012 m/s with a maximal wheel angular velocity of approximately 40 deg/s. The bin is 1.2 m long and 0.6 m wide while the soil depth is 0.16 m. Considering the wheel sizes and vertical loads under study, these physical dimensions are sufficient for eliminating boundary effects. Results presented in this paper were obtained with a smooth aluminum wheel with 0.13 m radius and 0.16 m width. For PIV tests the wheel angular velocity was fixed at 17 deg/s while the horizontal carriage velocity was modified to achieve the desired slip level. The operational conditions described above were chosen because they are close to those of the Mars Exploration Rover, a successful lightweight robotic vehicle.

2.2. Imager configuration

For the experiments described in this paper, the Mojave Martian Simulant (MMS) was employed as a test medium [16]. MMS is a mixture of finely crushed and sorted granular basalt intended to mimic, at both a chemical and mechanical level, Mars regolith characteristics. The MMS particle size distribution spans from micron level to mm level with 80% of particles above the 10 micron threshold. For the imager configuration described below, resolution resulted in approximately 5.3 pixels per millimeter.

The accuracy of PIV strongly depends on the quality of the captured images. For this study, the Lexan soil bin was fitted with a 0.0254 m thick tempered glass wall while the running gear was operated flush against this surface



Fig. 1. CAD drawing of the terramechanics testbed showing the imager for PIV experiments (a). Actual PIV setup with the high speed camera and two flood lights (b).

(see Fig. 1). Both wheels and tracks have been analyzed with this testbed, however this paper describes results from rigid wheel testing.

Since soil–glass friction could not be accurately controlled it should be noted that calculated velocities and strain, although quantitatively significant, are influenced by soil–glass friction. When setting up a similar experiment, Wong [13] proposed to use a wheel with half the width and to reduce the normal load to half as well. The rationale was that assuming negligible soil–glass friction the glass becomes a plane of symmetry and therefore the soil motion is analog to the motion under the median axis of a full sized wheel. In this paper we did not follow this route for two reasons: vertical load and wheel size do not scale linearly; even assuming linear scaling this would require wheels of different width for every vertical load to be tested. Therefore, assuming limited soil–glass friction and minor stress non-uniformity along wheel width [17], the soil motion at the glass interface remains representative of the soil motion under the wheel. These are insurmountable limitations of this methodology and should be borne in mind when analyzing the results. Nonetheless, the method allows for a quantitative evaluation of strain trends under running gears.

Image sets for the PIV measurement were captured with a Phantom 7 high-speed camera. The Phantom 7 is able to record grayscale images at the maximum resolution of 800x600 pixels at a maximum frame rate of 6688 fps. The camera was placed perpendicular to the front glass wall (see Fig. 1) at a distance of 0.52 m, while its focal length was set to 77 mm (a zoom lens was used) resulting in an image capture region of approximately 0.15×0.11 m. It should be noted that determination of image capture region size is largely dictated by the particular experimental conditions. Here, the image capture region was chosen in order to conservatively bound the region of soil that would undergo motion when subjected to wheel passage on the soil surface. Two 250 W Lowel Pro-Light photography flood lights were placed on either side of the camera at an angle of 45 towards the object plane, and provided approximately homogeneous illumination of the soil. By using two laterally positioned light sources, reflections and shadows can be significantly diminished.

PIV algorithms (as explained in Appendix A) compare group of pixels delimited by an interrogation window (IW). The optimization of IW size and frame rate again depends on particular experimental conditions. Here, the soil grain size and magnitude of soil velocity both directly influence required imager spatial (grain size) and temporal (image capture rate) resolution. Keane and Adrian [18] suggest that an average of 10 or more particles per interrogation window should be employed in order to maximize PIV algorithm accuracy. Also, they suggest that particle displacement should not exceed 25% of the IW length.

Particle packing density for granular materials can be estimated by detecting the number of particles in a reference area. A process to perform this computation can be divided into three parts. First, the grayscale image is transformed into a binary image via thresholding. Each cluster of pixels representing one particle is then reduced to one pixel by using a morphological shrinking operation (implemented with Matlabs `bwmorph-shrink` function). In this process, pixel clusters with internal holes are transformed into rings of pixels. Finally, the number of white pixels is summed over a chosen IW size, with ring artifacts counted as single pixels (see Fig. 2).

Assuming a minimum IW length of 16 pixels, this results in an IW area of 256 pixels, or approximately 11 particles, satisfying Keane and Adrians suggested guideline. Note that IWs containing fewer particles can be employed,

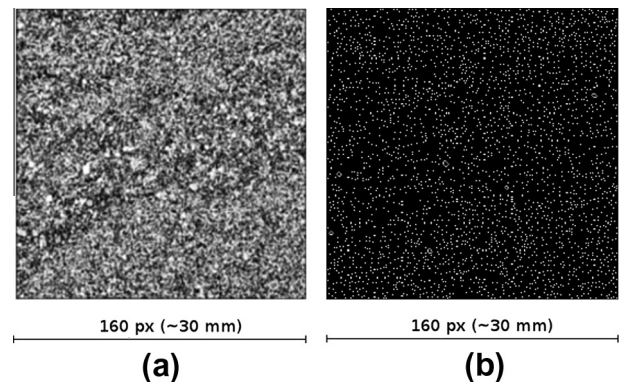


Fig. 2. Image transformation for particle counting. (a) Image segment before transformation. (b) Image segment after transformation.

however the result is a decrease in accuracy in frame-to-frame feature correlation. Generally, if particle density is unsatisfactorily low, the imager field of view can be adjusted to focus on a smaller spatial soil region.

The experiments analyzed soil motion for conditions where the wheel was driven at varying forward velocities and slip ratios. The maximum speed of a point on the wheel rim was computed to be 0.038 m/s. Given the imager parameters described above, this suggests that image capture rate of 25 fps should satisfy the condition that particle displacement should not exceed 25% of the IW length. Experiments were conducted to verify the effectiveness of selected conditions, and more broadly, analyze the effect of varying IW sizes and frame rates. The results of these studies are reported in [19].

The performance of PIV cross-correlation algorithms generally improves when images are high contrast, feature dense, and have low noise. In practice, images are subject to non-uniform illumination, imager sensor noise, and lack of natural contrast in the granular material, all of which can degrade PIV algorithm performance. Various image pre-processing methods were investigated to understand their effect on algorithm performance. These include commonly employed algorithms such as contrast limited adaptive histogram equalization (CLAHE), high pass filtering, and clipping and intensity capping (IC). It was determined that optimal performance were achieved with the following settings: CLAHE filter with size of 40 pixels, while all other filters were disabled.

Motion estimation can be improved through multi-pass PIV where the results of each pass are used to improve estimation of the IW in the next pass. Several multi-pass combinations were tested and a three-pass PIV calculation which use sequential IW sizes of 64, 32, and 16 pixels was determined to be a balanced compromise between improved accuracy and calculation times.

The raw velocity field produced by PIV calculations can contain spurious vectors (outliers). These outliers can be caused by noise, inappropriate interrogation settings, and accidentally matched patterns. Hence, to improve results, rejection of these outliers and interpolation of missing data points can be performed in a post-processing stage through filtering. In this study, both global and local filters were used to reject outliers. Global filters commonly employ a simple thresholding method, with the threshold value selected by an operator possessing empirical or theoretical domain knowledge. If elements of the velocity field exceed the threshold, this element is removed from the results. Local filters are primarily based on relative differences between surrounding vectors, rather than absolute values. A local filter calculates the mean and standard deviation of the velocity for a selected kernel size around each vector. If the velocity exceeds certain thresholds, the vector is rejected.

The filtering methods described above lead to missing data in the PIV velocity field. It is frequently desirable to interpolate missing data points, to yield a complete velocity

field. Interpolation based on surrounding vectors. For this purpose missing data points were reconstructed through interpolation of surrounding velocity vectors.

Final PIV settings adopted in this paper are presented in Table 1.

It should be noted that a masking stage has been employed in the results presented in this paper, in order to eliminate the non-soil image components (i.e. the running gear). Masking can be accomplished through standard image processing techniques. Masking methods specific to running gear–soil interaction are described in [19].

2.3. Computation times

This study was conducted on a Windows based 2.4 GHz quad-core machine with 4 GB of RAM. The complete PIV calculation for an average image set (about 13 s recording time) took approximately 60 min. More than two thirds of this time is spend on the main process, the multi-pass cross-correlation. Post-processing and the creation of the video file each consume roughly 7% of the total calculation time. Pre-processing takes only 3% of the total calculation time.

It should be noted that masking and creation of video files are two steps that are not inherently part of the PIV analysis and do not affect the quality of results. Calculation times are summarized in Table 2.

3. Validation and verification

Validation of the PIV algorithm performance was pursued on two sets of test data that were physically relevant to the running gear–soil interaction case.

The first test consisted in calculating the velocity from PIV of a 0.0254 m thick steel plate performing a soil penetration test. The ground truth velocity of the plate was externally measured by numerically differentiating the output of a draw wire encoder which nominally provides a position measurement. To obtain a plate velocity measure from PIV, an average of the velocities was computed over a rectangular region corresponding to the moving plate.

Fig. 3(a) shows a comparison of the plate velocity as determined from PIV calculations and the velocity measured by the draw wire encoder. The absolute average

Table 1
PIV settings.

Parameter	Value	Unit
Interrogation window (IW)	16	Pixels
Frames per second (fps)	25	fps
Resolution	800 × 600	Pixels
Frame size	0.15 × 0.11	m
CLAHE filter	40	Pixels
High pass filter	Off	n/a
Clipping filter	Off	n/a
Intensity capping filter	Off	n/a
Multi-pass IW sequence	64-32-16	Pixels

Table 2
Computation times.

Task	Time per image set (270 images) [s]	Time per image [s]	(%)
Masking	516	1.91	15
Pre-processing	112	0.41	3
Cross-correlation	2320	8.59	67
Post-processing	257	0.95	7
Creation of video file	256	0.95	7
Total time	3461	12.82	100

percent error (for the optimal settings) between these measurements was less than 3%. It should be noted that, for this test case, the PIV algorithm is not performing calculations on the granular soil, but rather the steel plate edge. However, this test remains of interest since the soil in contact with the plate necessarily moves at the same velocity.

The second test consisted of calculating the time evolution of motions of discrete features associated with MMS simulant soil beneath a driven rigid wheel (see Fig. 3(b)). Trajectories $s(t)$ are calculated for a grid of 9 x 6 points of interest over the soil area. The time evolution of the positions of the points of interest was computed by integrating the velocities with a fourth order Runge–Kutta method.

$$s(t) = \int_0^t v(t) dt \quad (1)$$

The motion of these tracked particles can be compared to trajectories of individual soil particles that are large enough to be manually tracked from frame to frame. Also, the calculation of feature trajectories is useful for illustrating soil flow when subjected to various loading conditions. When compared to non-digital techniques [13], PIV allows for systematic quantitative investigation of soil motion. In-depth discussion of observed soil kinematics will be presented in 5.

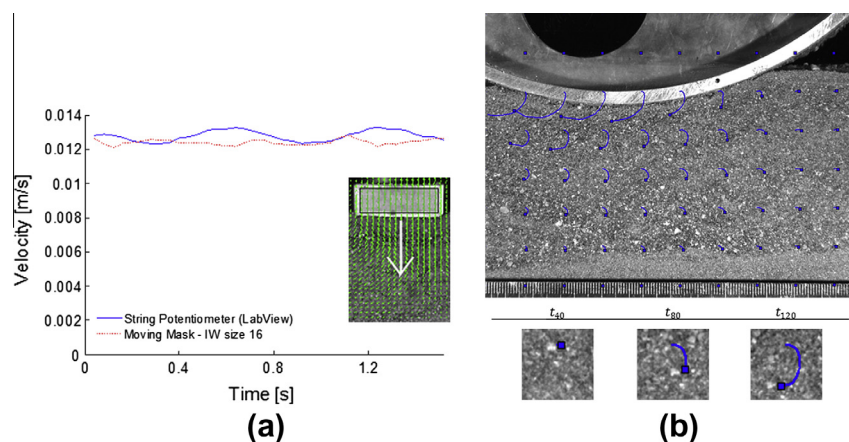


Fig. 3. (a) Comparison of velocity calculated through PIV and measured with a draw wire encoder. (b) Soil trajectories calculated from velocity field obtained through PIV analysis for a wheel slipping at +30% while advancing to the right of the field (right, bottom). A close up of a region of soil where a large, white particle, is tracked over successive images (images were captured at 25 fps).

4. Inferring strain from PIV measurements

The methodology presented thus far allows for precise calculation of soil motion. The approach yields displacement vectors from one captured image to the next at discrete pixels inside the image domain. The inferred displacements describe a motion of groups of particles. While this provides significant insight in terms of local material response, a more convenient quantity to report is strain.

Here, the material strain is calculated in a Lagrange reference frame using a large-strain finite element-based approach [20–22]. Specifically, we initialize a fixed set of material points, conveniently defined as the nodal points of a finite element mesh at a chosen reference configuration. The nodal points are subsequently tracked in time, as they progress through a grid of incremental PIV displacements. This approach is favoured over local image-based methods because of the extreme plastic nature of (most) soil materials. In particular, the ability of soil to undergo large plastic deformations arising from microstructural rearrangement means that PIV must be applied in an incremental fashion (and not with respect to a single image reference).

Below are briefly summarized the non-trivial steps involved in extracting local strains from PIV measurements (as summarized in Fig. 4). All calculations and visualization were performed in Matlab2012b using an in-house program built for the purpose.

1. A finite element mesh is used to fill the domain occupied by soil. To this end, we use four-node quadrilateral elements (rather than constant-strain triangular elements) to insure a continuous strain field. The element size is on the order of 8x8 pixels.
2. At each imaged time step, incremental displacements of all nodes in the finite element mesh are interpolated from PIV results using bi-linear shape functions. The

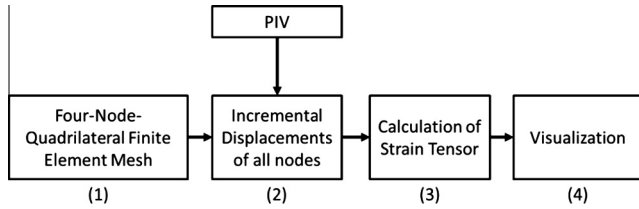


Fig. 4. Schematic flowchart of strain calculation from PIV data.

Table 3

Summary of data collected. Each test was repeated for -30% , -10% , 0% , 10% , and 30% slip. Wheel diameter is 0.13 m and wheel width is 0.16 m for all the experiments.

Test type	Load [N]	Label
Coated wheel standard	70	Std low load
Velocity loose soil	100	Std medium load
	130	Std High Load
Coated wheel standard velocity dense soil	130	Dense high load
Coated wheel double velocity loose soil	130	2 V high load
Smooth wheel standard velocity loose soil	130	Loose high load

Table A.4

Summary of image canonical transformations adopted to investigate PIV performance.

Frames	Transformation
1–4	Diagonal translation (positive), 1 to 4 pixels
5–8	Diagonal translation (negative), 1 to 4 pixels
9–12	Horizontal translation, 1 to 4 pixels
13–16	Horizontal simple shear, 1 to 4 pixels
17–20	Vertical displacement, 1 to 4 pixels
21–24	Vertical simple shear, 1 to 4 pixels
25–32	Rotation 1 to 8 degrees
33–36	Discontinuous shear (upper half moving, 1 to 4 pixels)
37–40	Discontinuous shear (both halves moving in opposite directions, 1 to 4 pixels)

process is repeated for all time steps, yielding the cumulative displacements at finite element nodes as a function of time.

- To determine strain, at each of the 4 Gauss points inside an element, nodal quantities are first converted to a deformation gradient tensor $\mathbf{F} = d\mathbf{x}/d\mathbf{X}$, that relates a vector $d\mathbf{x}$ in the deformed state with a vector $d\mathbf{X}$ in the reference state. The deformation gradient tensor is calculated based on the gradients of the finite element shape functions. Subsequently, a large strain (Green–Lagrange) tensor is calculated, such that $\mathbf{E} = \mathbf{F}^T\mathbf{F} - \mathbf{I}$, where \mathbf{I} is a unit tensor. Deviatoric (shear) strain is defined as $\epsilon_s = \sqrt{4J_2/3}$, where J_2 is the second deviatoric strain invariant.
- To visualize the strain field, Gauss point strains are first transferred back to element nodes and their magnitude is subsequently plotted over the entire (meshed) domain using standard element shape functions. Because a continuous mesh describes the soil, the technique makes it

possible to visualize material deformation, and at the same time, visualize the local strain state in the deformed finite element mesh.

Representative results of PIV-based strain calculations are provided in Figs. 8, 9.

5. Application to analysis of running gear–soil interaction

Typically, analysis of running-gear soil interaction relies on the use of a single wheel (or track) test rig that is capable of measuring performance parameters such as applied load, torque, slip ratio, and net thrust. While useful, such testing does not provide fundamental insight into soil motion and failure, nor does it allow for explicit validation of constitutive laws relating soil stress to displacement. Granular PIV can be employed as a complementary testing apparatus to a single wheel test rig. In this section we present several simple PIV-based analysis and visualization tools for characterizing soil response to loading. The tests are conducted under controlled slip conditions. Slip is defined as:

$$i = 1 - \frac{v}{\omega r} \quad (2)$$

where v is the translational velocity of the wheel, ω is the angular velocity of the wheel, and r is wheel radius. By modifying v and keeping ω constant, it is possible to drive the wheel at desired slip level. In results presented here, the wheel was coated with a layer of MMS bonded to the surface with spray glue while tests were performed at 70 N, 100 N, and 130 N of vertical load (labeled low, medium, and high load). The wheel was driven at a constant angular velocity of 17 deg/s, while for higher velocity tests angular velocity was set to 34 deg/s (these tests were labeled 2 V). Testing conditions are summarized in Table 3. For all the figures presented in this paper, the wheel is moving from the left to the right. (See Table A.4)

5.1. Characterization of soil velocity field

The PIV algorithm generates a velocity vector for each IW, which results in a closely-spaced array of vectors describing soil motion. An example visualization of such a result is shown in Fig. 5 (top left). Here, each IW is associated to a vector, with the vector length corresponding to the flow velocity and the vector direction aligned with the flow direction. Analysis of such images can provide insight into the spatial distribution of soil velocity under running gear, and can vary dramatically for such cases as slip, skid, free-rolling wheels, braked wheels, etc.

Decomposition of this flow field can yield useful insight into soil shearing (which occurs primarily in the horizontal direction, see upper right image) and soil compaction phenomena (which occurs primarily in the vertical direction, see upper right image). Here, a blue region corresponds to no motion while red indicates a maximum velocity.

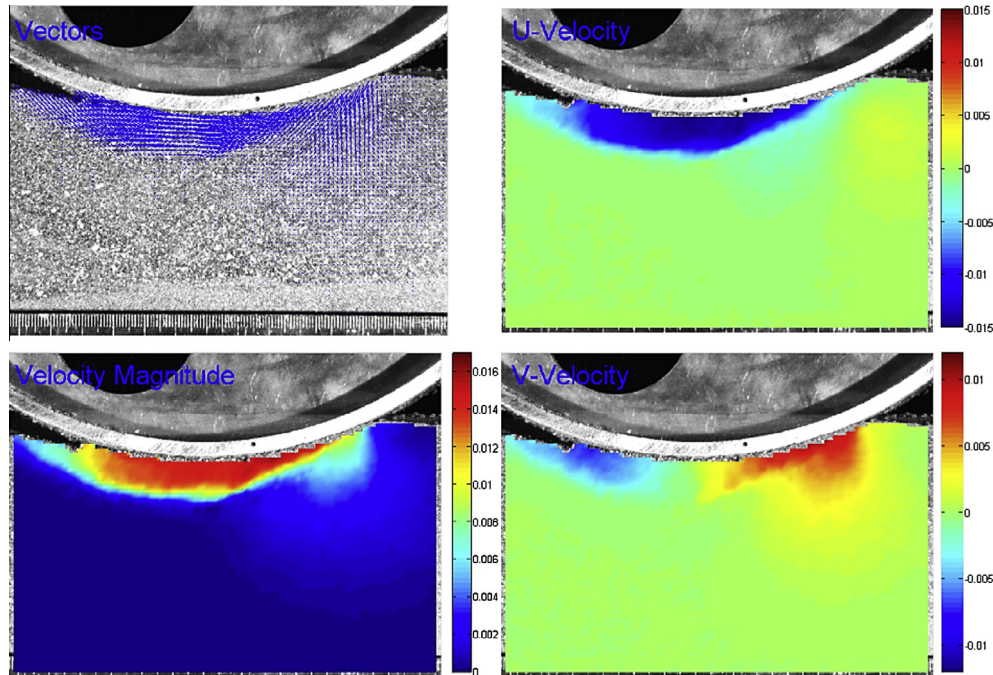


Fig. 5. A snapshot of a 30% slip test (Std High Load). Nominal vertical load is 100 N and wheel angular velocity 17 deg/s. From top-left-clockwise: velocity vectors, u-velocity (horizontal component of velocity vector, negative is left), v-velocity (vertical component of velocity vector, negative is up), and velocity magnitude.

Another phenomenon that was clearly highlighted by PIV analysis is the periodic nature of soil failure. For slip level above 10–15%, soil exhibits a periodic loading cycle of alternating compaction and shearing (behavior is primarily dilatative during the shearing phase), which results in discontinuous failure in of the soil mass. This has two direct consequences: oscillations in drawbar pull/torque readings, and creation of ripples on the soil surface behind the wheel. Note that while these effects have been noted previously, they have been typically assigned to the effect of grousers [23]. However, these effects are present even for smooth wheels, without grousers. Fig. 6 presents soil flow mean velocity for a +30% slip test. Mean velocity oscillation capture the periodic nature of soil failure and are clearly visible also in the torque signal.

Analysis of these images shows that soil flow remains attached to the wheel rim. Moreover, for low vertical load (such as the one utilized during experiments) it was observed that two separate slip failure lines did not evolve, as predicted by classical theory [24,25]. This finding is interesting because according to [24], the maximum stress occurs where the soil flow separates. Also, for slip levels below $\pm 10\%$, the soil was not observed to develop a significant shearing plane.

5.2. Characterization of soil failure

Traditionally, soil failure under running gear has been considered as an analog of failure under a strip load [26]. Following the analogy, two time-independent failure zones were predicted under the wheel. A basic approach for

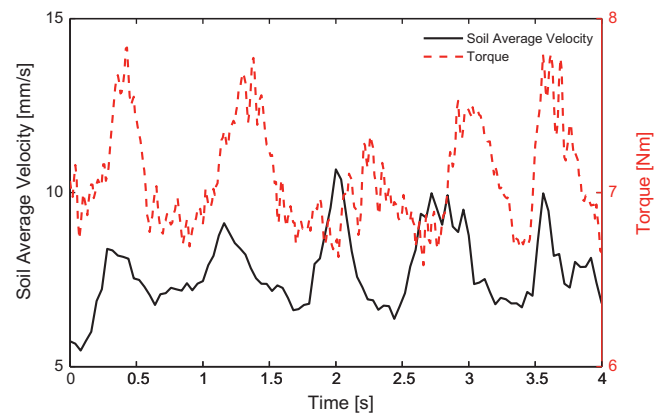


Fig. 6. Periodicity of failure zone for a coated wheel under 100 N of vertical load and +30% slip (Std High Load) is evident when visualizing soil mean velocity and wheel torque reading. This figure is obtained calculating the average velocity of soil motion per frame. The periodicity occurs at about 2 Hz. Torque reading was not sampled synchronously with images therefore a phase shift between the two signals may exist even if here they have been plotted in phase. Nevertheless, it is remarkable that such close correlation between the two quantities exists, indicating that the measured wheel telemetry could potentially be used to improve estimation of soil properties below surface and vice versa.

shearing plane identification is to define it based on velocity magnitude: the deepest point in the soil, where the velocity is above a specified threshold, is identified in each column. A polynomial curve is fitted to these points. Fifth order polynomials were used to interpolate the data, since lower-order representations produced poor results, while higher order representations did not improve significantly

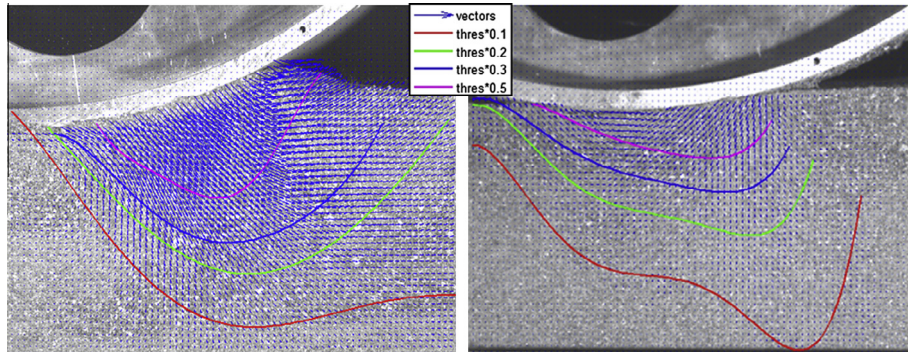


Fig. 7. Visualization of shearing planes for a -30% (left) and a $+30\%$ (right) slipping wheel (Std High Load). Shearing planes are detected through a line scanning algorithm and the extension of the sheared area depends on the threshold chosen. Because of soil periodic failure, shearing planes are time-varying features. Best viewed in color. (For interpretation of the references to colour in this figure legend, the reader is referred to the web version of this article.)

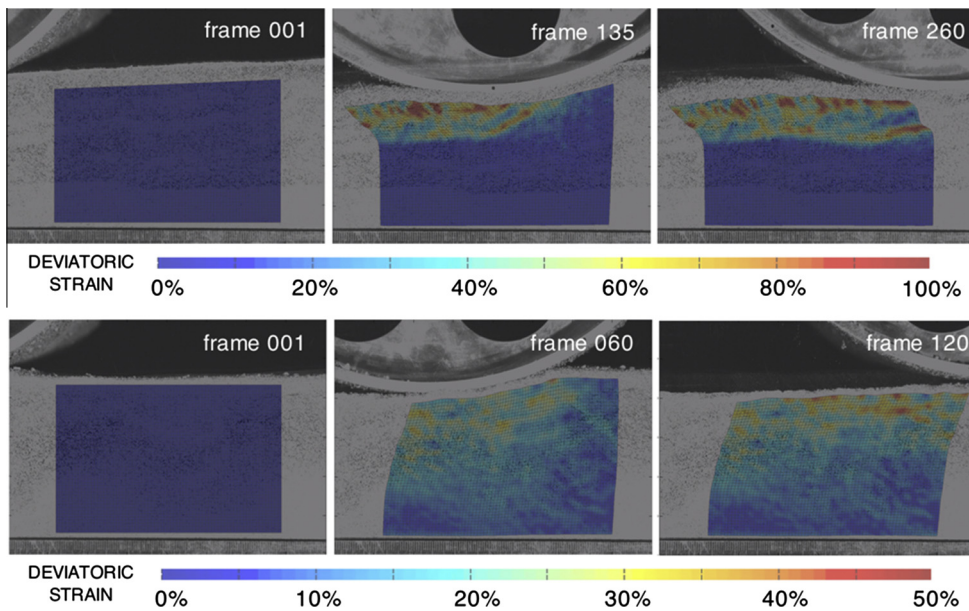


Fig. 8. (Top) Cumulative deviatoric (shear) strain at different time instants for positive $+30\%$ wheel slip (Std High Load). (Bottom) Cumulative deviatoric (shear) strain at different time instants for negative -30% wheel slip. The depth and magnitude of soil disturbance for positive (top) and negative (bottom) wheel slip indicate markedly different soil responses.

the result. According to classical theory, shearing failure is thought to occur along a logarithm spiral, however it was not possible to confirm this experimentally.

Identification of a shearing plane depends on the specified velocity threshold. Fig. 7 presents images for -30% (left) and $+30\%$ (right) wheel slip, for various velocity thresholds. It is interesting to note that for both slip level, there exists only a single shearing plane. However, it should be noted that soil under the wheel is not continuously failing, and therefore shearing planes are typically time-varying features.

A more systematic way to study the failure zone is to calculate soil strain as presented in Section 4. Calculation of strain allows for quantitative description of shear bands and enables more detailed description of soil evolution. Fig. 8 shows a “strain imprint” left behind by a wheel as it travels across the image domain. The depth and

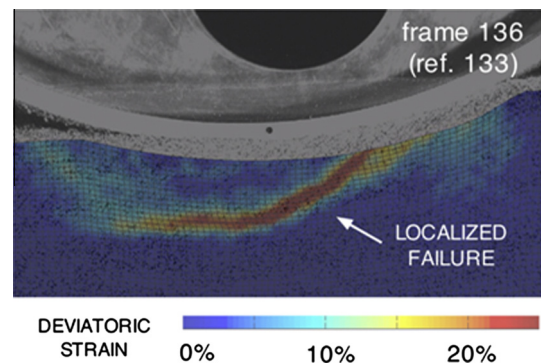


Fig. 9. Total deviatoric (shear) strain over 4 time steps, showing localized failure region under the wheel. Strain is shown with respect to reference frame 133, rather than frame 1 as in other the strain plots of Fig. 8. A localized shear band is clearly visible. It should be noted that soil under the wheel is not continuously failing, and therefore failure bands are typically time-varying features.

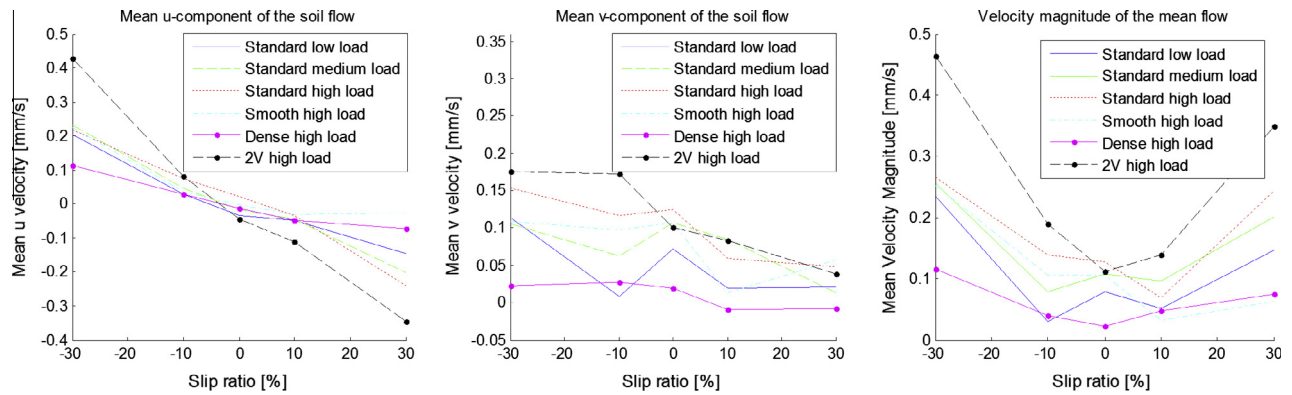


Fig. 10. Horizontal (left), vertical (center), and magnitude (right) of mean flow velocity for slip values ranging from -30% up to $+30\%$. These metrics summarize the results obtained for different soil preparation (dense and loose), different wheel velocity (17 deg/s and 34 deg/s), different vertical load (70 N , 100 N , and 130 N), and different wheel surface finish (smooth and coated with MMS). Note that for dense soil and smooth wheel only one series of experiments (at 17 deg/s and 100 N of vertical load) was conducted. Data is obtained by averaging soil motion measured over all the IWs where motion was detected.

magnitude of soil disturbance for positive (top) and negative (bottom) wheel slip indicate markedly different soil responses for positive and negative wheel slip conditions. Positive wheel slip produces a shallower soil disturbance, with a clear transition between the disturbed and undisturbed soil regions.

For 30% positive slip, the largest accumulated strains can easily surpass 100% , owing to localized failure of the material. In contrast, for -30% wheel slip, no localized soil failures are observed, with soil deformation distributed over a much deeper portion of material, and the largest accumulated strains consistently below 50% . In both cases, after the wheel has passed, a complex deformation (strain) field is left behind.

In order to visualize shear band formation it is beneficial to isolate a reference frame. This is presented in Fig. 9 where strain, for a 30% slipping wheel, is calculated over 4 frames. The starting frame (i.e. the reference frame), is conveniently chosen just prior to shear band initiation. This allows one to highlight localized shear failure of the granular material during positive wheel slip with the wheel positioned roughly in the center of the image for a better field of view. These localized failures occur at periodic intervals, as highlighted in Fig. 6.

5.3. Motion metrics

To grossly summarize results obtained from PIV analysis, a series of qualitative metrics was developed. The mean horizontal velocity, mean vertical velocity, and mean magnitude velocity were calculated for each frame, and again over the entire experiment duration. These metrics are intended to give a “snapshot” of collected data and reveal the key trends of soil motion. Results for the experiments described in Table 3, are presented as function of slip in Fig. 10.

For standard velocity tests, the u-velocity ranges between -0.2 mm/s and 0.2 mm/s . The u-component

vanishes for 0% slip, where the horizontal motion is caused solely by compressive motion of the soil, which pushes equally to both directions. Dense soil yields a lower horizontal velocity independent of the slip ratio, while experiments with the smooth wheel result in reduced horizontal velocity for high positive slip, due to wheel slip at the wheel-soil interface (and thus reduced soil shearing). For doubled rotational velocity, the horizontal component of the mean flow is approximately doubled (Fig. 10, left). This is intuitively reasonable, because the relative velocity between wheel and soil beneath the wheel axle depends proportionally on the rotational velocity. The vertical component of the mean flow shows a generally declining trend from negative to positive slip ratios. By increasing the weight, the vertical velocity increases, as illustrated in tests with the coated wheel in Fig. 10(center). Dense soil causes significantly reduced vertical flow. An unexpected trend is shown by all standard tests for 0% slip: The vertical velocity increases compared to -10% .

In these tests, each experiment was performed once and averaging was performed over all frames of that experiment. Experimental variation is likely due to variable soil conditions, despite the fact that an identical soil preparation process was performed for each run. Soil was stirred with a rod and then leveled. When higher density was desired, terrain was compacted with a cylindrical roller. This procedure guaranteed consistent soil preparations at large scale.

6. Conclusions

This paper shows how granular particle image velocimetry can enable investigation of running gear–soil interaction phenomena. This type of analysis can allow for development of improved constitutive models for granular materials, and for development of reduced order models based on soil displacement predictions. An important consideration to bear in mind when examining flow fields like

the one presented in Fig. 5, is that the relationship between stress and displacement is typically complex, and one must avoid the temptation to directly correlate velocity magnitudes with stress magnitudes.

This paper presented a detailed description of granular particle image velocimetry methodology for analyzing soil flow under running gears. Although this approach is confined to plain strain analysis, it enables detailed quantitative and qualitative analysis of soil failure patterns.

A procedure for systematically determining operational parameters for PIV analysis was presented. The natural texture of the granular, dry, material under investigation was found to be sufficient for PIV analysis eliminating the need of markers.

For the experimental setup under investigation it was found that only a contrast limited adaptive histogram equalization (CLAHE) pre-processing filter (set to 40 pixels) was necessary while the best interrogation windows and multi-pass sequence was found to be 64–32–16 (corresponding to IW size, in pixels, for first, second, and third pass). Post-processing strategies for outlier detection and substitution based on local and global filters were presented as well. The methodology utilized in this paper to determine the best blend of settings could be in theory utilized with any type of soil and imager setup.

It was shown that velocity fields calculated through granular PIV can be successfully utilized to infer strain fields. Experimental results show that it is possible to compute, with satisfactory accuracy, soil motion characteristics. A series of controlled-slip wheel experiments was performed and analyzed with the proposed methodology highlighting complex soil failure patterns.

Further investigation of small robot-terrain interaction mechanics will focus on extending these experiments to a wider range of vertical loads. This will provide a basis for characterization of soil plastic internal variable, validation of constitutive laws, and, ultimately, the improvement of reduced-order models.

Acknowledgements

This study was partially supported by the U.S. Army Tank Automotive Research, Development and Engineering Center (TARDEC). The Workshop on “xTerramechanics – Integrated Simulation of Planetary Surface Missions”, sponsored by the Keck Institute for Space Studies at California Institute of Technology (August 2011), has been inspirational to the crafting of this research. The authors are grateful to Michele Judd, the managing director of the Keck Institute for Space Studies, to Dr. James W. Bales, the assistant director of the Edgerton Center at MIT, and to A. Sarafraz, J. D’Errico, and W. Thielicke.

Appendix A. Steps for PIV

Soil motion analysis can be broken down into three main steps: (1) image pre-processing, (2) image cross-correlation,

and (3) velocity field post-processing. Each step is briefly described and methods for parameter selection are presented.

A.1. Image pre-processing

Various image pre-processing methods were investigated to understand their effect on algorithm performance. These include commonly employed algorithms such as contrast limited adaptive histogram equalization (CLAHE), high pass filtering, and clipping and intensity capping (IC).

CLAHE differs from basic histogram equalization in two aspects. First, it computes several histograms, each for a separate region of the original image, and thus operates on local parts of the image. Additionally, by limiting the contrast amplification for a given pixel value, it prevents addition of noise to the images. The contrast of images used for PIV has a significant influence on the shape of the correlation plane, which is used for estimation of the velocities. Hence, pre-processing of the images by optimizing contrast can improve the performance of PIV calculations [27].

High pass filtering reduces low-frequency image intensity fluctuations. A high pass filter can remove the background artifacts that are of a lower frequency than the natural particle texture, and is usually carried out by performing basic multiplications on the image in the frequency domain.

Clipping itself is not a pre-processing filter to increase image quality, but rather a method to increase the computation speed through determination of irrelevant areas for the PIV calculation.

Intensity capping attempts to reject local image intensities which differ too much from their surrounding environment, and could thus degrade the accuracy of the PIV by causing bias.

To systematically investigate the effect of these pre-processing methods on PIV algorithm performance, test image segments of the Mars regolith simulant with dimensions 256×256 pixels were captured, and then synthetically deformed in canonical directions. Since the particle distribution in the soil under investigation is locally not perfectly homogeneous, two distinct image segments were captured in order to adequately represent common grain appearance in the MMS simulant. This resulted in one image populated by relatively large grains (Fig. A.11(a)) and one populated by relatively small grains (Fig. A.11(b)). Synthetic deformation of the image was performed as a means of generating a ground truth for cases of linear translation (1–4 pixels in both horizontal, vertical, and diagonal directions), rotation (1–8 degrees in clockwise and counter-clockwise directions), shear (1–4 pixels of relative motion between upper and lower image halves), and simple shear (1–4 pixels of motion of the upper edge of image) (see Figs. A.12, A.13).

A total of 40 transformed images was produced. Since the pixel shift for each deformation was controlled, this

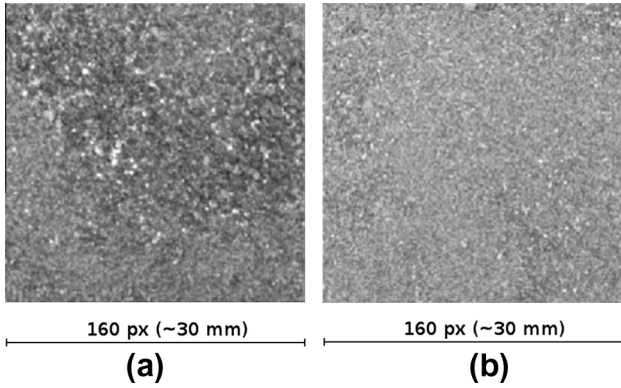


Fig. A.11. Examples of soil natural textures: coarse (a) and fine (b).

methodology allowed quantitative evaluation of PIV algorithm results. A relative error metric was defined as following:

$$\epsilon = \frac{1}{2N} \sum_i^N (u_i - u_{iPIV})^2 + (v_i - v_{iPIV})^2 \tag{A.1}$$

where u_i, v_i are the true velocity components (based on controlled image transformation) at image location i , and u_{iPIV}, v_{iPIV} are the velocity components, for the same spatial location, estimated through PIV analysis. This is essentially an average mean square error. When the cross-correlation algorithm is not able to calculate a velocity, it returns a NaN value. The error metrics does not account for NaN values, however the number of NaNs is monitored to allow for a comprehensive evaluation of algorithm performance.

The forty synthetically deformed images were analyzed under various combinations of pre-processing settings. In total, 96 different combinations of pre-processing parameters were studied (see Appendix B for details on pre-processing parameter combinations).

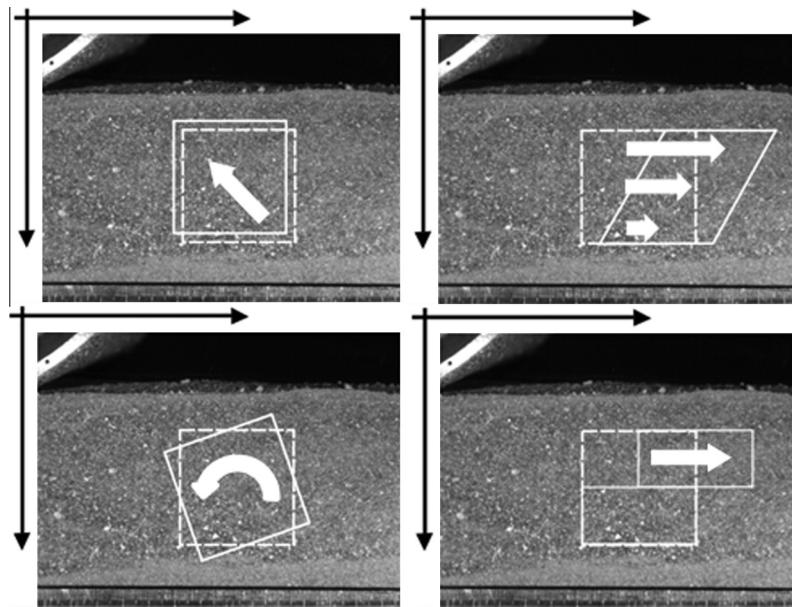


Fig. A.12. Examples of image canonical transformations used to evaluate PIV settings. Nine image transformations for coarse and fine soil textures were used to evaluate PIV accuracy. Transformations included: rigid translation (upper-left), simple shear (upper-right), rigid rotation (bottom-left), and discontinuous shear (bottom-right). Details in Table A.4.

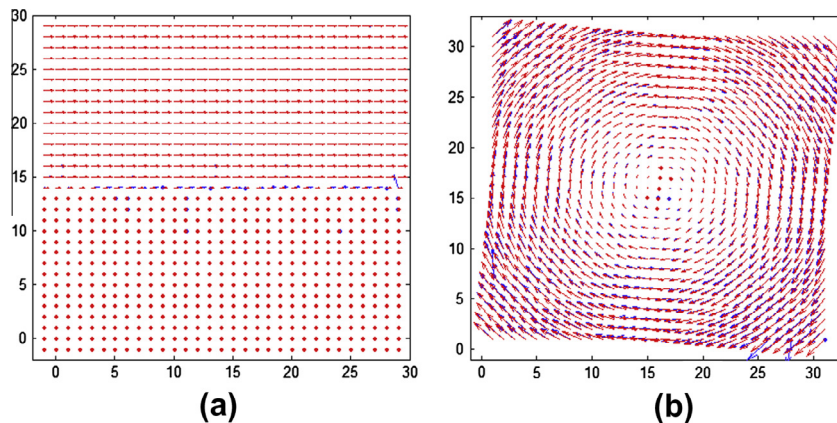


Fig. A.13. Velocity field for image transformation, discontinuous shear (a) and rotation (b). Largest error occurs at peak velocity gradient.

These tests were conducted using an IW size of 16×16 pixels. Generally, it was observed that the largest errors occurred in shear tests at the simulated failure plane (i.e. the plane of relative motion between the top and bottom halves of the image), as shown in Fig. A.12. For rotation and simple shear, the largest errors occurred at the image borders (see Fig. A.13).

Overall, the accuracy of the PIV calculations was found to be good even without any pre-processing method applied. The high level of performance was attributed to the natural, significant intensity variation present in the MMS simulant, the carefully controlled lighting conditions, and the proper selection of imager configuration.

Fig. A.14(a) shows the averaged (over all frames) mean square error for all the settings. Employing a CLAHE filter with filter sizes of 20 and 40 was found to reduce the mean square error. The use of a high pass filter was found to be uniformly detrimental to PIV calculation accuracy while a clipping filter was found to be effectively negligible. Intensity capping had a varying effect on accuracy, depending on the other pre-processing settings, however its influence was small when other settings are judiciously chosen. Examining the other dimension of the test space, it can be seen that the mean square error was influenced significantly by the different image transformation (Fig. A.14(b)).

Generally, linear translation deformations could be accurately estimated with a wide range of algorithm parameter settings, whereas rotational transformations resulted in larger errors. Averaged mean square error for all the frames (Fig. A.14(a)) is usually small because cross-correlation works particularly well with rigid translation which represent most of the transformations.

As Fig. A.14(b) shows, the highest error levels are observed during rotation and shear (i.e., when relatively high velocity gradients are present). Those results can be contextualized by noting that the ground truth velocity for the synthetically deformed images ranged between 0 and 8 pixels/frame. Although the average square error is in the order of 0.1 pixels²/frame², the maximum error reaches 3 pixels²/frame² for the most unfavorable (but not physically unreasonable) conditions.

Although the use of setting # 73 caused relative error to improve only marginally compared to un-preprocessed images, it was found that the PIV algorithm produced fewer NaN returns (i.e., areas where the displacement could not be estimated) with this setting, therefore # 73 was adopted. A complete description of the image/pre-processing parameter combinations and results are presented in [19].

A.2. Image cross-correlation (PIV)

In PIV, images are divided into small interrogation windows (IW) and then analyzed to compute the probable displacement between successive images for each IW using cross-correlation techniques. This results in an equally

spaced field of calculated velocity vectors. The probable displacement is determined by using the cross-correlation function:

$$R_{II^*}(x, y) = \sum_{i=-K}^K \sum_{j=-L}^L I(i, j) I^*(i + x, j + y) \quad (\text{A.2})$$

where I is the intensity of the first image and I^* the intensity of the second image [28]. As noted in Section 2.1, particle packing density, image resolution, and IW size are interconnected parameters that must carefully selected to optimize performance. Based on experimental investigations, Keane and Adrian [18] defined four empirical rules for optimal PIV setup. First, the number of particles per IW, N_I , should be more than 10:

$$N_I > 10. \quad (\text{A.3})$$

In-plane particle motion can lead to an inability to compute cross-correlation across image pairs, because of the reduction of correlation between particle intensities in both images. Hence, the particle displacement X_I should not exceed a 25% of the IW length L :

$$X_I < \frac{1}{4} L. \quad (\text{A.4})$$

Out-of-plane soil motion can cause particles to leave the visible plane and appear/disappear in different images. This effect again leads to an inability to compute cross-correlation across image pairs. For granular PIV, however, it is typically impossible to explicitly control out-of-plane soil motion. Instead, experiments should be designed in order to minimize out-of-plane soil flow.

PIV methods compute a velocity vector for an area of particles. Since the soil particle velocity in this area is usually not constant, the computed velocity represents an average of the velocities of all particles within the area. High gradients in the velocity field will cause the peak in the correlation-plane to broaden. As a guiding rule, the maximum difference of displacement, a , should not exceed the average particle size d_t , and also be below 5% of the IW length L :

$$a = |X_{I,max} - X_{I,min}| \\ a < d_t \quad a < 0.05L. \quad (\text{A.5})$$

It should be noted that while enlarging the IW size may allow for better cross-correlation performance, larger IWs result in greater spatial averaging of the flow velocities. Also, the maximum displacement that can be measured depends on the size of the IWs. (The smaller the chosen IWs are, the shorter the measurable displacement.) Ideally, the IW size is chosen to measure the maximum frame-to-frame displacement, while minimizing spatial averaging, and yielding good cross-correlation performance. When selection of a static IW size that yields good performance can be difficult, multi-pass PIV can be employed to achieve improved performance.

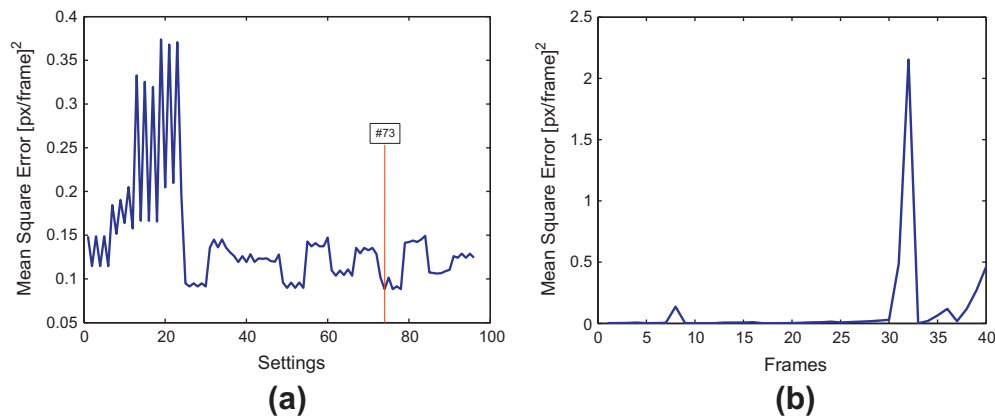


Fig. A.14. Pre-processing test space was bi-dimensional: 40 frames \times 96 pre-processing settings. Fig. A.14(a) presents the mean square error averaged over all frames. Setting #73 (see Appendix B) was chosen to be the optimal choice because of the good balance of performance (low error and low number of NaN). Fig. A.14(b) shows the mean square error for pre-processing settings # 73 over all the synthetically deformed images. Performance deteriorates for high velocity/velocity gradient corresponding to rigid rotation and shear frames (see Table A.4).

A.2.1. Multi-pass PIV

In multi-pass PIV, multiple PIV calculations are performed successively, where the results of each pass are used to improve estimation of the IW in the next pass.

This can yield improved performance at the cost of additional computation. The simplest approach to multi-pass PIV relies on a repetitive determination of a static window offset for each IW, which is based on the calculated velocity from the prior pass [29].

The multi-pass settings that were evaluated are displayed in Table A.5. The IW size for each pass was varied between 16 pixels and 64 pixels, while the last pass was always performed with the previously determined optimum IW size (i.e., 16 pixels). A maximum of four passes was tested. These tests were executed on the previously described synthetically deformed images and the error is reported as mean square error over all the frames for pre-processing setting # 73.

The mean square error of the velocities computed from PIV compared to the actual velocities is displayed in Fig. A.15. As expected, the use of multi-pass led to improved performance at the expense of increased processing times. Error can be reduced by approximately an order of magnitude when moving from single-pass PIV (setting # 9) to multi-pass. Note that although the minimum errors were observed for settings # 1, 3, 5 setting # 4 (a three pass calculation) was selected as optimal because it required approximately 30% less computation time while still showing a significant improvement with respect to the single pass setting # 9. To further reduce computation at a cost of modestly reduced accuracy, setting # 7 can be employed (a two pass calculation) (see Fig. A.15). Note that the times presented in Fig. A.15 represent wall clock times for the PIV calculations running on a 2.4 GHz quad-core desktop PC (although the code was not parallelized and Matlab used only one core). A three-pass PIV calculation (setting # 4), which uses sequential IW sizes of 64, 32, and 16 pixels was considered a balanced choice between accuracy and computation times.

A.3. Velocity field post-processing

The raw velocity field produced by PIV calculations can contain spurious vectors (outliers). These outliers can be caused by noise, inappropriate interrogation settings, and accidentally matched patterns. Hence, to improve results, rejection of these outliers and interpolation of missing data points can be performed in a post-processing stage through filtering. Filters for the rejection of outliers can primarily be divided into two separate classes: global and local methods.

Global filters commonly employ a simple thresholding method, with the threshold value selected by an operator possessing empirical or theoretical domain knowledge. If elements of the velocity field exceed the threshold, this element is removed from the results.

For granular PIV, a global threshold can be defined as a maximum speed for which it is known that no flow vector will physically exceed. For the case of running gear–soil interaction, such a velocity can be determined by computing the maximum velocity, calculated in an inertial frame, of points lying on the running gear itself. For non-dynamic tests (i.e. with negligible impact forces), it can be assumed that no element of the flow field will have a velocity greater than the maximum running gear velocity.

Local filters are primarily based on relative differences between surrounding vectors, rather than absolute values.

Table A.5
Multi-pass settings. Units are in pixels.

Setting #	1st IW	2nd IW	3rd IW	4th IW
1	64	32	16	16
2	64	32	32	16
3	64	16	16	–
4	64	32	16	–
5	32	16	16	–
6	32	32	16	–
7	64	16	–	–
8	32	16	–	–
9	16	–	–	–

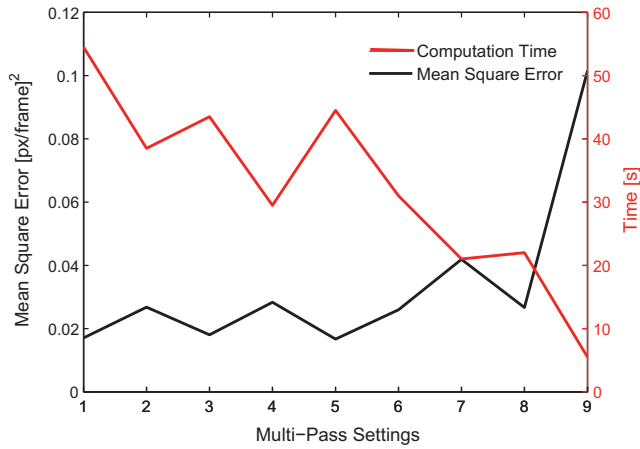


Fig. A.15. Mean square error and computation time for different multi-pass settings. Setting # 9, based on a single pass, produces the worst result. On the right, computation time for different multi-pass settings.

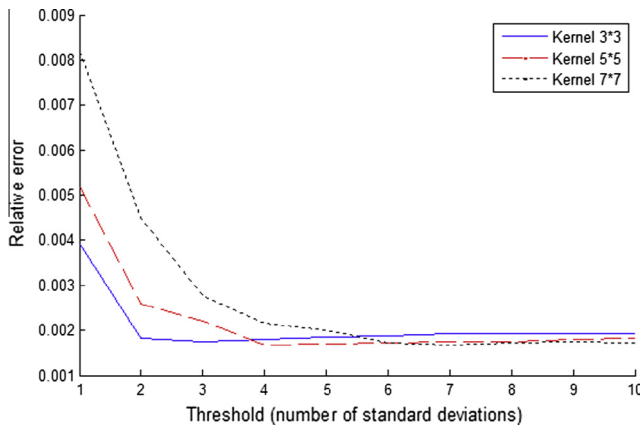
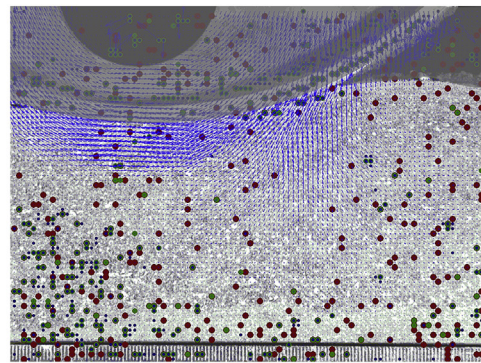
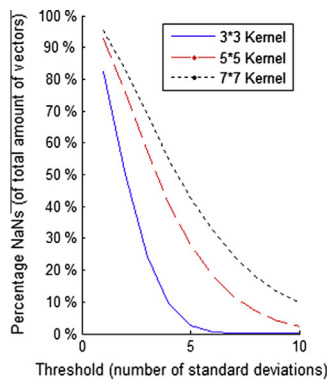


Fig. A.16. Mean square error for different post-processing kernel sizes and threshold settings. These results were obtained for pre-processing settings # 73 and the synthetically deformed images. High relative error for low thresholds is caused by rejection of a high number of vectors (see Fig. A.17, where a wheel experiment is presented). However, even for threshold that produces low error, it is necessary to verify the number of rejected vectors in order to produce balanced results.



A local filter calculates the mean and standard deviation of the velocity for a selected kernel size around each vector. If the velocity exceeds certain thresholds, the vector is rejected.

Thresholds are defined by the mean velocity plus or minus a number of standard deviations. Such a filter typically operates on the u and v velocity components separately:

$$\begin{aligned}
 u_{max} &= u_{mean} + ku_{std} \\
 u_{min} &= u_{mean} - ku_{std} \\
 v_{max} &= v_{mean} + kv_{std} \\
 v_{min} &= v_{mean} - kv_{std}.
 \end{aligned}
 \tag{A.6}$$

The effect of local filter settings on PIV performance was investigated for the synthetically deformed images. Three different kernel sizes (3×3 , 5×5 , and 7×7 pixels) were tested with thresholds ranging from 1–10 standard deviations. The mean square error over these settings is shown in Fig. A.16.

Error decreased for all kernel sizes while the number of standard deviations increased the accuracy for lower thresholds. Increasing the number of standard deviations also results in fewer rejected vectors, as displayed in Fig. A.17(a), where a wheel experiment is presented.

The large errors observed for low thresholds are a consequence of rejecting non-spurious vectors. By increasing the threshold, a point of minimum error is reached between 2–6 standard deviations, depending on the filter size. Error tends to increase for higher thresholds, due to the fact that some outliers are retained, which decreases accuracy. It should be noted that larger kernel sizes lead to higher computational cost, since they require more calculations per vector under consideration.

A.4. Interpolation of missing data points

The filtering methods described above lead to missing data in the PIV velocity field. It is frequently desirable to

Fig. A.17. (a) Percentage of rejected vectors for different threshold and kernel size obtained for a +30% slipping wheel Fig. (A.17(b)). For 7×7 kernel size, even at high threshold, a significant portion of vectors are rejected. Partial results are overlaid on the right image. Color legend is as follow. Red, kernel size 3×3 threshold 4; Green, kernel size 5×5 threshold 8; Blue, kernel size 7×7 threshold 10. Images considered for error analysis were masked to eliminate non-soil regions from the image. (For interpretation of the references to colour in this figure legend, the reader is referred to the web version of this article.)

interpolate missing data points, to yield a complete velocity field. Two interpolation approaches are described here: replacement with alternative correlation peaks, and interpolation based on surrounding vectors.

Spurious correlation results may be caused by a peak in the correlation plane that is higher than the peak corresponding to the real displacement. In this case, the peak corresponding to the real displacement may still exist in the correlation plane. Hence, the rejected vector should be replaced by an alternative correlation peak, if this data is available. For this reason, it is common to compute lower peaks, and thus if the highest peak does not correspond to the true displacement, a lower peak can be employed. Vectors computed from alternative peaks must then be filtered again, to ensure that they are consistent with respect to the surrounding flow field.

If information about lower correlation peaks is not available, missing data in the flow field must be interpolated in a different manner. The simplest interpolation method is linear interpolation. The value of the currently missing vector is simply replaced by information from neighbouring vectors:

$$U_i = \frac{1}{2}(U_{i-1} + U_{i+1}). \tag{A.7}$$

Other interpolation methods can be employed based on non-linear expressions. Furthermore, it is possible to build an over-determined system for the local area, and approximate the missing vector with a least squares approach [30]. It should be noted that while spatial filtering and interpolation has been discussed here, similar methods can be employed for temporal filtering. Due to space constraints this discussion is omitted.

Appendix B. Pre-processing settings

Table B.6.

Table B.6

Pre-processing settings.

Test	CLAHE	High pass	Clipping	IC
1	off	off	off	off
2	off	off	off	on
3	off	off	5	off
4	off	off	5	on
5	off	off	10	off
6	off	off	10	on
7	off	5	off	off
8	off	5	off	on
9	off	5	5	off
10	off	5	5	on
11	off	5	10	off
12	off	5	10	on
13	off	15	off	off
14	off	15	off	on
15	off	15	5	off

16	off	15	5	on
17	off	15	10	off
18	off	15	10	on
19	off	30	off	off
20	off	30	off	on
21	off	30	5	off
22	off	30	5	on
23	off	30	10	off
24	off	30	10	on
25	10	off	off	off
26	10	off	off	on
27	10	off	5	off
28	10	off	5	on
29	10	off	10	off
30	10	off	10	on
31	10	5	off	off
32	10	5	off	on
33	10	5	5	off
34	10	5	5	on
35	10	5	10	off
36	10	5	10	on
37	10	15	off	off
38	10	15	off	on
39	10	15	5	off
40	10	15	5	on
41	10	15	10	off
42	10	15	10	on
43	10	30	off	off
44	10	30	off	on
45	10	30	5	off
46	10	30	5	on
47	10	30	10	off
48	10	30	10	on
49	20	off	off	off
50	20	off	off	on
51	20	off	5	off
2	20	off	5	on
53	20	off	10	off
54	20	off	10	on
55	20	5	off	off
56	20	5	off	on
57	20	5	5	off
58	20	5	5	on
59	20	5	10	off
60	20	5	10	on
61	20	15	off	off
62	20	15	off	on
63	20	15	5	off
64	20	15	5	on
65	20	15	10	off
66	20	15	10	on
67	20	30	off	off
68	20	30	off	on
69	20	30	5	off
70	20	30	5	on
71	20	30	10	off
72	20	30	10	on
73	40	off	off	off
74	40	off	off	on
75	40	off	5	off
76	40	off	5	on
77	40	off	10	off
78	40	off	10	on
79	40	5	off	off
80	40	5	off	on
81	40	5	5	off

82	40	5	5	on
83	40	5	10	off
84	40	5	10	on
85	40	15	off	off
86	40	15	off	on
87	40	15	5	off
88	40	15	5	on
89	40	15	10	off
90	40	15	10	on
91	40	30	off	off
92	40	30	off	on
93	40	30	5	off
94	40	30	5	on
95	40	30	10	off
96	40	30	10	on

References

- [1] Lauterborn W, Vogel A. Modern optical techniques in fluid mechanics. *Annu Rev Fluid Mech* 1984;16:223–44.
- [2] Dudderar T, Meynart R, Simpkins P. Full-field laser metrology for fluid velocity measurement. *Opt Lasers Eng* 1988;9(3–4):163–99. doi:10.1016/S0143-8166(98)90002-1. <http://www.sciencedirect.com/science/article/pii/S0143816698900021>.
- [3] Buchhave P. Particle image velocimetry status and trends. *Exp Therm Fluid Sci* 1992;5(5):586–604. Special Issue on Experimental Methods in Thermal and Fluid Science. doi:10.1016/0894-1777(92)90016-X. <http://www.sciencedirect.com/science/article/pii/089417779290016X>.
- [4] Adrian R. Twenty years of particle image velocimetry. *Exp Fluids* 2005;39(2):159–69.
- [5] Sveen J, Cowen E. Quantitative imaging techniques and their application to wavy flows. *Adv Coastal Ocean Eng* 2004;9:1.
- [6] Sielamowicz I, Błoński S, Kowalewski T. Digital particle image velocimetry (dpiv) technique in measurements of granular material flows, part 2 of 3-converging hoppers. *Chem Eng Sci* 2006;61(16):5307–17.
- [7] Jain N, Ottino J, Lueptow R. An experimental study of the flowing granular layer in a rotating tumbler. *Phys Fluids* 2002;14:572.
- [8] Pudasaini S, Hsiau S, Wang Y, Hutter K. Velocity measurements in dry granular avalanches using particle image velocimetry technique and comparison with theoretical predictions. *Phys Fluids* 2005;17:093301.
- [9] Barnett C, Bengough A, McKenzie B. Quantitative image analysis of earthworm-mediated soil displacement. *Biol Fertil Soils* 2009;45(8):821–8.
- [10] Winter A. Biologically inspired mechanisms for burrowing in undersea substrates. Ph.D. thesis, Massachusetts Institute of Technology; 2011.
- [11] Saengprachatanarug K, Ueno M, Taira E, Okayasu T. Modeling of soil displacement and soil strain distribution under a traveling wheel. *J Terramech* 2012.
- [12] Moreland S, Skonieczny K, Wettergreen D, Creager C, Asnani V. Soil motion analysis system for examining wheel-soil shearing. In: 17th International conference for the society of terrain-vehicle systems; 2011.
- [13] Wong J. Behaviour of soil beneath rigid wheels. *J Agric Eng Res* 1967;12(4):257–69.
- [14] Thielicke W, Stamhuis EJ. PIVlab – time-resolved digital particle image velocimetry tool for matlab. <http://pivlab.blogspot.com/>.
- [15] Iagnemma K, Shibly H, Dubowsky S. A laboratory single wheel testbed for studying planetary rover wheel-terrain interaction. MIT field and space robotics laboratory technical report 1; 2005. p. 05–05.
- [16] Beegle LW, Peters GH, Mungas GS, Bearman GH, Smith JA, Anderson RC. Mojave martian simulant: a new martian soil simulant. In: Lunar and planetary institute science conference abstracts; 2007.
- [17] Senatore C, Wulfmeier M, MacLennan J, Jayakumar P, Iagnemma K. Investigation of stress and failure in granular soils for lightweight robotic vehicle applications. In: Proceedings of NDIA ground vehicle systems engineering and technology symposium modeling & simulation, testing and validation (MSTV) mini-symposium, Troy, MI; 2012.
- [18] Keane R, Adrian R. Theory of cross-correlation analysis of piv images. *Appl Sci Res* 1992;49(3):191–215.
- [19] Wulfmeier M. Development of a particle image velocimetry method for analysis of mars rover wheel-terrain interaction phenomena. b.S. thesis, Gottfried Wilhelm Leibniz Universitaet Hannover; April 2012.
- [20] Zienkiewicz O, Taylor R. The finite element method: solid mechanics. Finite Element Method Series, vol. 2. Oxford [etc.]; Butterworth Heinemann; 2000. <http://books.google.com/books?id=MhgBfMWFV-HUC>.
- [21] Bazant ZP. Finite strain generalization of small-strain constitutive relations for any finite strain tensor and additive volumetric-deviatoric split. *Int J Solids Struct* 1996;33(20):2887–97. [http://dx.doi.org/10.1016/0020-7683\(96\)00002-9](http://dx.doi.org/10.1016/0020-7683(96)00002-9). <http://www.ingentaconnect.com/content/els/00207683/1996/00000033/00000020/art00002>.
- [22] Ibrahimbegovic A. Nonlinear solid mechanics: theoretical formulations and finite element solution methods. *Solid Mech Appl*. Springer; 2009. <http://books.google.com/books?id=z8oI0hCMt40C>.
- [23] Ding L, Gao H, Deng Z, Nagatani K, Yoshida K. Experimental study and analysis on driving wheels' performance for planetary exploration rovers moving in deformable soil. *J Terramech* 2011;48(1):27–45. <http://dx.doi.org/10.1016/j.jterra.2010.08.001>. <http://www.sciencedirect.com/science/article/B6V56-50XRXF0-1/2/ac7e7af600ac1856641535f01c8e1900>.
- [24] Wong JY. Theory of ground vehicles. 3rd ed. New York: John Wiley & Sons; 2001.
- [25] Karafiath LL, Nowatzki EA. Soil mechanics for off-road vehicle engineering. Clausthal, Germany: Trans Tech Publications; 1978.
- [26] Bekker MG. Off-the-road locomotion; research and development in terramechanics. Ann Arbor: The University of Michigan Press; 1960.
- [27] Dellenback P, Macharivilakathu J, Pierce S. Contrast-enhancement techniques for particle-image velocimetry. *Appl Opt* 2000;39(32):5978–90.
- [28] Adrian R, Westerweel J. Particle image velocimetry. Cambridge University Press; 2010. vol. 30.
- [29] Westerweel J. Fundamentals of digital particle image velocimetry. *Measure Sci Technol* 1999;8(12):1379.
- [30] Currell G, Dowman A. Essential mathematics and statistics for science. Wiley; 2009.